A Bayesian Approach to Eigenspectra Optoacoustic Tomography

Ivan Olefir, Stratis Tzoumas, Hong Yang, and Vasilis Ntziachristos*

***Abstract*— The quantification of hemoglobin oxygen saturation (sO_2) with multispectral optoacoustic (photoacoustic) tomography (MSOT) is a complex spectral unmixing problem, since the optoacoustic spectra of hemoglobin are modified with tissue depth due to depth (location) and wavelength dependencies of optical fluence in tissue. In a recent work, a method termed eigenspectra MSOT (eMSOT) was proposed for addressing the dependence of spectra on fluence and quantifying blood sO_2 in deep tissue. While eMSOT offers enhanced sO_2 quantification accuracy over conventional unmixing methods, its performance may be compromised by noise and image reconstruction artifacts. In this work, we propose a novel Bayesian method to improve eMSOT performance in noisy environments. We introduce a spectral reliability map, i.e. a method that can estimate the level of noise superimposed onto the recorded optoacoustic spectra. Using this noise estimate, we formulate eMSOT as a Bayesian inverse problem where the inversion constraints are based on probabilistic graphical models. Results based on numerical simulations indicate that the proposed method offers improved accuracy and robustness under high noise levels due the adaptive nature of the Bayesian method.**

***Index Terms* — Optoacoustic/photoacoustic imaging, multispectral optoacoustic tomography, photoacoustic tomography, Bayesian methods, oxygen saturation, spectral unmixing.**

I. Introduction

TISSUE blood oxygenation is a significant physiological marker of tissue viability, metabolism, hypoxia [1] and even neuronal activation [2]. By unmixing the absorption spectra of oxygenated and deoxygenated hemoglobin, multispectral optoacoustic tomography (MSOT) can produce label-free images of blood oxygenation (sO_2) of tissue *in vivo*, at high spatial and temporal resolution [3, 4]. However, accurate quantification of blood sO_2 in deep tissue in MSOT presents a complex spectral unmixing problem, since the measured optoacoustic (OA) spectrum from a tissue volume element (voxel) depends not only on the local concentration of different photoabsorbers but also on the wavelength-dependent optical fluence reaching that voxel. This effect is known as *spectral coloring* [5-7] or *spectral corruption*.

In recent work [8], a novel method termed eigenspectra MSOT (eMSOT) was proposed for accounting for spectral coloring and quantitatively estimating blood sO_2 deep within tissue in the near-infrared (NIR) region. The method is based on the observation that any fluence spectrum recorded in tissue in NIR can be modelled based on four base spectra (eigenspectra), assuming oxygenated and deoxygenated hemoglobin as the two prominent NIR absorbers. The eigenspectra were derived by applying principal component analysis (PCA) to a set of simulated optical fluence spectra, which served as the training dataset. Modelling the light fluence spectrum as a linear combination of the four eigenspectra converts the fluence correction problem from the spatial domain to the spectral domain. Then the sO_2 MSOT estimation problem can be written as a spectral unmixing problem that is dependent on the scalar weights of the linearly combined eigenspectra but independent of the tissue's optical properties. By accounting for the effects of *spectral coloring*, eMSOT has been shown to offer substantially enhanced sO_2 estimation accuracy over the linear unmixing technique in simulations, phantoms and animal measurements [8], especially as tissue depth increases.

In addition to spectral coloring, optoacoustic spectra may also be corrupted due to noise and artifacts present in the images [9], compromising eMSOT convergence and accurate sO_2 estimation. In this work, we aimed to improve the accuracy of sO_2 quantification by eMSOT under noise conditions. To achieve this aim, we formulate the eMSOT sO_2 quantification problem as a Bayesian inverse problem where the noise in the recorded spectra is taken into account. Noise estimation is carried out by considering a new model that describes the recorded optoacoustic spectra and captures their variability due to both light fluence and hemoglobin absorption. Based on this model of recorded optoacoustic spectra we introduce the *spectral reliability map (SRM)* as an estimator of the noise in the measurements. In the SRM-enabled Bayesian eMSOT (BeMSOT), the original inversion constraints are modeled as prior probability distributions and implemented using probabilistic graphical models. We show how the parameters of the prior probability distributions affect the accuracy of sO_2 quantification by BeMSOT and optimize their values using simulated data. Results based on simulations indicate that the proposed method offers more robust sO_2 quantification than eMSOT in the presence of high and non-uniform noise levels, due to the ability of the Bayesian formulation to reduce the impact of unreliable data on algorithm performance.

In the following, we describe the methodology and findings by providing the physical background of optoacoustics and

The research leading to these results has received funding by the Deutsche Forschungsgemeinschaft (DFG), Sonderforschungsbereich-824 (SFB-824), subproject A1 and Gottfried Wilhelm Leibniz Prize 2013 (NT 3/10-1).

Ivan Olefir, Hong Yang and Vasilis Ntziachristos are with the Institute for Biological and Medical Imaging (IBMI), Helmholtz Zentrum München, Neuherberg, Germany; and Chair of Biological Imaging, Technische Universität München. München, Germany (e-mails: ivan.olefir@helmholtz-muenchen.de, hong.yang@helmholtz-muenchen.de, v.ntziachristos@tum.de)

Stratis Tzoumas is with the Department of Radiation Oncology, School of Medicine, Stanford University, Stanford, USA (e-mail: stzoumas@stanford.edu)

*Correspondence to Vasilis Ntziachristos (v.ntziachristos@tum.de)

theoretical background of eMSOT (Section II), formulating the eMSOT algorithm as a Bayesian Maximum a Posteriori (MAP) estimation problem (Section III-A), and introducing the novel SRM noise estimator (Section III-B). Simulations are described in Section III-C. In Section IV (Results), we assess the performance of the noise estimation technique and BeMSOT. Finally, Section V (Discussion) places the findings in the perspective of future challenges and developments.

II. Background

A. Physics of Optoacoustics. Forward and Inverse Problems

In MSOT, a nanosecond laser pulse illuminates tissue at multiple wavelengths. Due to thermoelastic expansion caused by light absorption, this results in an *initial pressure rise* (IPR) p which relates to the fluence Φ and tissue absorption coefficient μ_a as follows [10]:

$$p(\mathbf{r},\lambda) = \Gamma(\mathbf{r})\Phi(\mathbf{r},\lambda)\mu_a(\mathbf{r},\lambda), \tag{1}$$

where $\mathbf{r}$ denotes the spatial coordinates, λ is the illumination wavelength, p is the space- and wavelength-dependent initial pressure and Γ is the spatially varying Grüneisen parameter. The generated ultrasound waves subsequently exit the tissue and propagate towards the acoustic detectors.

Due to the hybrid nature of optoacoustics, the forward and inverse problems are two-fold:

- *Optical forward problem* – compute $\mathbf{\Phi}$ when the optical properties of the medium and illumination are known.
- *Acoustic forward problem* – compute the time-dependent pressure signals $\mathbf{s}_{\text{pr}}$ on the detectors around the sample given the initial pressure rise $\mathbf{p}$.
- *Acoustic inverse problem* – reconstruct optoacoustic images $p(\mathbf{r},\lambda)$ given the detector signals $\mathbf{s}_{\text{pr}}$.
- *Optical inverse problem* – determine the spatial distribution of the optical properties within the sample given the map of the initial pressure rise.

Accounting for $\Phi(\mathbf{r},\lambda)$ and computing $\mu_a(\mathbf{r},\lambda)$, or solving the *optical inverse problem*, is the key challenge in quantitative optoacoustics.

A multitude of approaches to solving the inverse optical problem have been considered [11-22]. Typically, the solution is computed by inverting a discretized optical forward model under certain assumptions (e.g. some of the optical parameters being known). The forward model is governed by ether the Radiative Transfer Equation [11, 18, 19, 21, 22] or less computationally expensive Diffusion Approximation [11-14, 16, 17, 19]:

$$\begin{aligned} &-\nabla\kappa(\mathbf{r},\lambda)\nabla\Phi(\mathbf{r},\lambda)+\mu_a(\mathbf{r},\lambda)\Phi(\mathbf{r},\lambda)=0, r\in\Omega,\\ &\xi_d\Phi(\mathbf{r},\lambda)+\frac{1}{2}A\kappa(\mathbf{r},\lambda)\nabla\Phi(\mathbf{r},\lambda)\cdot\nu=s, r\in\partial\Omega, \end{aligned} \tag{2}$$

where Ω is the tissue region, $\partial\Omega$ is the tissue boundary, $\kappa(\mathbf{r},\lambda)=\left(d\left(\mu_a(\mathbf{r},\lambda)+\mu'_s(\mathbf{r},\lambda)\right)\right)^{-1}$ is the diffusion coefficient, d is the dimensionality of the domain, μ'_s is the reduced scattering coefficient; ξ_d is a dimensionality-dependent parameter; A describes reflectivity and s is the illumination pattern. The inversion may be performed for one as well as several wavelengths simultaneously.

Such approaches, although theoretically accurate, are however limited by several factors [19]. First, since the optical fluence is modeled accurately in the whole domain, the knowledge of the initial pressure rise in the illuminated volume is required, i.e. accurate image reconstruction is an important prerequisite for the described methods. Such reconstruction is often not achievable, and various artifacts as well as spatially inhomogeneous noise are typically present in the OA images. Second, due to the inverse problem being physics-driven, the absolute values of the absorbed energy density $\Phi(\mathbf{r},\lambda)\mu_a(\mathbf{r},\lambda)$ are required, which necessitates calibration for various scaling factors including the Grüneisen parameter as well as knowledge of accurate tissue boundary and illumination. Finally, due to a large number of unknowns, the resulting computational complexity of the problem is very high. The mentioned challenges effectively limit application of such methods to experimental data.

In contrast, eMSOT presents a simpler, although less versatile, alternative to the aforementioned approaches. It utilizes a linear spectral model of fluence (the eigenspectra model), converts the inverse problem to lie in the spectral domain and allows local fluence correction while avoiding modelling light transport in the inversion step. Instead of computing the distributions of the optical properties within the sample, eMSOT directly quantifies sO_2, making its application to experimental data possible [8].

B. The Eigenspectra Model

The Eigenspectra model is derived based on the assumption that oxygenated and deoxygenated hemoglobin are the main absorbers in tissue in the NIR region (700-900 nm) and that the influence of other absorbers can be neglected. Thus, Eq. 1 can be rewritten as:

$$\begin{aligned} p(\mathbf{r},\lambda) &= C(\mathbf{r})\Phi'(\mathbf{r},\lambda)\\ &\cdot\left(c_{\text{HHb}}(\mathbf{r})\varepsilon_{\text{HHb}}(\lambda)+c_{\text{HbO2}}(\mathbf{r})\varepsilon_{\text{HbO2}}(\lambda)\right)=\\ &\Phi'(\mathbf{r},\lambda)\cdot\left(c'_{\text{HHb}}(\mathbf{r})\varepsilon_{\text{HHb}}(\lambda)+c'_{\text{HbO2}}(\mathbf{r})\varepsilon_{\text{HbO2}}(\lambda)\right). \end{aligned} \tag{3}$$

where $\Phi'(\mathbf{r},\lambda)=\Phi(\mathbf{r},\lambda)/\|\mathbf{\Phi}(\mathbf{r})\|_2$ is the normalized fluence spectrum; $\|\mathbf{\Phi}(\mathbf{r})\|_2$ is the l_2-norm of the optical fluence spectrum at position $\mathbf{r}$; $C(\mathbf{r})=\Gamma(\mathbf{r})\|\mathbf{\Phi}(\mathbf{r})\|_2$; c_{HHb} and c_{HbO2} are the concentrations of deoxy- and oxyhemoglobin, respectively; $c'_{\text{HHb}}=C\cdot c_{\text{HHb}}$ and $c'_{\text{HbO2}}=C\cdot c_{\text{HbO2}}$ are relative concentrations; and ε_{HHb} and $\varepsilon_{\text{HbO2}}$ are the corresponding wavelength-dependent absorption coefficients. To exclude $C(\mathbf{r})$ from consideration, eMSOT operates on normalized initial pressure spectra (or simply *normalized OA spectra*), i.e. $\mathbf{p}'(\mathbf{r})=\mathbf{p}(\mathbf{r})/\|\mathbf{p}(\mathbf{r})\|_2$. If the relative concentrations can be found, sO_2 can be computed as:

$$sO_2 = \frac{c_{\mathrm{HbO2}}}{c_{\mathrm{HbO2}} + c_{\mathrm{HHb}}} = \frac{c'_{\mathrm{HbO2}}}{c'_{\mathrm{HbO2}} + c'_{\mathrm{HHb}}}. \quad (4)$$

In eMSOT, $\Phi'(\mathbf{r}, \lambda)$ is modeled as a linear function of four base spectra derived from PCA of a training dataset of simulated fluence spectra (see [8]):

$$\Phi'(\mathbf{r}, \lambda) = \Phi_{\mathrm{M}}(\lambda) + \sum_{i=1}^{3} m_{\mathrm{i}}(\mathbf{r}) \Phi_{\mathrm{i}}(\lambda), \quad (5)$$

where $\Phi_{\mathrm{M}}(\lambda)$ is the mean spectrum in the training data, $\Phi_{\mathrm{i}}(\lambda), i = 1...3$ are the principal components, and m_i are scalars referred to as *the eigenfluence parameters*. If $\boldsymbol{\theta} = (m_1, m_2, m_3, c'_{\mathrm{HHb}}, c'_{\mathrm{HbO2}})$, the eigenspectra model $\hat{p}(\mathbf{r}, \lambda, \boldsymbol{\theta})$ that approximates the normalized OA spectrum $p'(\mathbf{r}, \lambda)$ takes the following form:

$$\hat{p}(\mathbf{r}, \lambda, \boldsymbol{\theta}) = \left(\Phi_{\mathrm{M}}(\lambda) + \sum_{i=1}^{3} m_{\mathrm{i}}(\mathbf{r}) \Phi_{\mathrm{i}}(\lambda) \right) \cdot \left(c'_{\mathrm{HHb}}(\mathbf{r}) \varepsilon_{\mathrm{HHb}}(\lambda) + c'_{\mathrm{HbO2}}(\mathbf{r}) \varepsilon_{\mathrm{HbO2}}(\lambda) \right). \quad (6)$$

C. eMSOT Inversion

eMSOT is formulated as a constrained minimization problem in which the goal is to identify the values of a set of parameters $\boldsymbol{\theta}_{\mathrm{opt}}$ that minimize the second norm of the difference between the measured normalized spectrum $\mathbf{p}'(\mathbf{r})$ and the modeled $\hat{\mathbf{p}}(\mathbf{r}, \boldsymbol{\theta})$. The inversion is performed simultaneously for several selected spatially distributed spectra. The locations of the spectra are determined by a circular grid $\mathbf{G} = \left\{ \mathbf{r}^{(k,l)} \mid k = 1...n_{\mathrm{ln}}, l = 1...n_{\mathrm{pt}} \right\}$ of n_{ln} lines, each consisting of n_{pt} pixels, that is assigned to a region of interest (ROI) in the MSOT image. (Fig. 1 shows an example of such a grid.) A detailed overview of eMSOT inversion can be found in Supplementary Materials and [8].

III. METHODS

A. Formulation of the BeMSOT inverse problem

The eMSOT inversion described in Section II-B has been shown to provide more accurate sO_2 quantification in simulations and phantoms than commonly used linear unmixing, and it has been successfully applied in measurements of small animals [8]. However, these validation studies made clear that eMSOT accuracy is sensitive to noise in the data. In order to make eMSOT more robust to noise and thereby improve its overall accuracy, we hypothesized that we could estimate the noise in the MSOT data and, then, use that information in Bayesian-based eMSOT inversion (BeMSOT) to refine the quantification accuracy.

In the following, we will consider the eMSOT inverse problem in a Bayesian framework. The inverse problem will therefore be treated as a problem of statistical inference and the variables will be treated as random variables. It will be shown that, in contrast to sO_2 quantification using eMSOT, which uses no information on the quality of the measured normalized OA spectra, in the resulting problem of MAP estimation the noise in the measurements is taken into account. All inversion constraints in BeMSOT are formulated using probabilistic graphical models.

A.1. Bayesian formulation of eMSOT inversion

We denote as $\mathbf{P}'_{\mathrm{measured}}$ the vector of $n_\lambda n_{\mathrm{ln}} n_{\mathrm{pt}} \times 1$ measured normalized OA spectra on a grid $\mathbf{G}$ of points selected for inversion, where $n_\lambda = 21$ is the number of wavelengths. We denote the set of five unknown variables for every spectrum $(m_1, m_2, m_3, c'_{\mathrm{HHb}}, c'_{\mathrm{HbO2}})$ as $\boldsymbol{\Theta}$ with dimensions $n_{\mathrm{ln}} \times n_{\mathrm{pt}} \times 5$. $\boldsymbol{\Theta}$ can be written as $\boldsymbol{\Theta} = (\mathbf{M}_1, \mathbf{M}_2, \mathbf{M}_3, \mathbf{C}_{\mathrm{HHb}}, \mathbf{C}_{\mathrm{HbO2}})$, where $\mathbf{M}_i$ denotes the set of all m_i parameters for all grid points, i.e. $\mathbf{M}_{\mathrm{i}} = \left\{ m_i^{(k,l)} \mid k = 1...n_{\mathrm{ln}}, l = 1...n_{\mathrm{pt}} \right\}$, and $\mathbf{C}_{\mathrm{HHb}}$ and $\mathbf{C}_{\mathrm{HbO2}}$ are defined analogously. Elements of $\boldsymbol{\Theta}$ can be referred to based on their linear index (e.g. $\mathbf{M}_1^{(i)}, i = 1...n_{\mathrm{ln}} \times n_{\mathrm{pt}}$) or their node $\mathbf{r}$ in the grid (e.g. $\mathbf{M}_1^{(\mathbf{r})}, \mathbf{r} \in \mathbf{G}$).

Under the assumption of additive noise $\mathbf{E}$, the observation model is written as follows:

$$\mathbf{P}'_{\mathrm{measured}} = \mathbf{P}_{\mathbf{model}}(\boldsymbol{\Theta}) + \mathbf{E}, \quad (7)$$

where $\mathbf{P}_{\mathbf{model}}(\boldsymbol{\Theta})$ denotes the eigenspectra model that corresponds to the measurements. The solution to the inverse problem is the posterior probability $\pi(\boldsymbol{\Theta} \mid \mathbf{P}'_{\mathrm{measured}})$, which, according to the Bayes' formula, can be written in terms of conditional probabilities as follows [23]:

$$\pi(\boldsymbol{\Theta} \mid \mathbf{P}'_{\mathrm{measured}}) = \frac{\pi(\mathbf{P}'_{\mathrm{measured}} \mid \boldsymbol{\Theta}) \pi(\boldsymbol{\Theta})}{\pi(\mathbf{P}'_{\mathrm{measured}})}, \quad (8)$$

where $\pi(\mathbf{P}'_{\mathrm{measured}} \mid \boldsymbol{\Theta})$ is the data likelihood and $\pi(\boldsymbol{\Theta})$ is the prior probability. $\pi(\mathbf{P}'_{\mathrm{measured}})$ is fixed for a given measurement $\mathbf{P}'_{\mathrm{measured}}$, therefore Eq. 8 can be used in a nonnormalized form:

$$\pi(\boldsymbol{\Theta} \mid \mathbf{P}'_{\mathrm{measured}}) \propto \pi(\mathbf{P}'_{\mathrm{measured}} \mid \boldsymbol{\Theta}) \pi(\boldsymbol{\Theta}), \quad (9)$$

We will consider a pointwise estimate of $\boldsymbol{\Theta}$, more specifically, a maximum a posteriori estimate $\boldsymbol{\Theta}_{\mathbf{MAP}}$:

$$\boldsymbol{\Theta}_{\mathbf{MAP}} = \arg\max_{\boldsymbol{\Theta}} \pi(\boldsymbol{\Theta} \mid \mathbf{P}'_{\mathrm{measured}}), \quad (10)$$

In the following subsections, we define models for data likelihood and prior distribution for BeMSOT inversion.

A.2. Data Likelihood in BeMSOT

Under the assumption of noise and $\boldsymbol{\Theta}$ being independent, Eq. 7 leads to the likelihood density [23, 24]:

$$\pi(\mathbf{P}'_{\mathrm{measured}} \mid \boldsymbol{\Theta}) = \pi_N(\mathbf{P}'_{\mathrm{measured}} - \mathbf{P}_{\mathbf{model}}(\boldsymbol{\Theta})), \quad (11)$$

where π_N denotes the probability distribution of noise. If $\mathbf{N}$ is Gaussian noise with zero mean and covariance matrix $\mathbf{\Sigma}$, Eq. 11 becomes:

$$\pi\left(\mathbf{P}'_{\text{measured}} \mid \mathbf{\Theta}\right) \propto \exp\left(-\left\|\mathbf{P}'_{\text{measured}} - \mathbf{P}_{\mathbf{model}}(\mathbf{\Theta})\right\|^2_{\mathbf{\Sigma}}\right), \quad (12)$$

where $\|\mathbf{x}\|^2_{\mathbf{\Sigma}} = \mathbf{x}^{\mathbf{T}}\mathbf{\Sigma}\mathbf{x}$. We assume that $\mathbf{\Sigma}$ is a diagonal matrix with dimensions $n_\lambda n_{\text{ln}} n_{\text{pt}} \times n_\lambda n_{\text{ln}} n_{\text{pt}}$ in which each non-zero entry equals the variance of noise at a specific wavelength in a specific spectrum. $\mathbf{\Sigma}$ (or $\mathbf{\Sigma}^{-1}$) can be estimated using the method described in Section III-B .

A.3. Prior Distributions of Unknown Parameters

Defining the prior probability distribution is an essential part of MAP estimation approach [25]. The prior distributions reflect the available knowledge on the expected values of the unknown parameters.

Assuming the sets of unknown variables are independent of one another, $\pi(\mathbf{\Theta})$ can be expressed as

$$\pi(\mathbf{\Theta}) = \pi(\mathbf{C}_{\text{HHb}})\pi(\mathbf{C}_{\text{HbO2}})\prod_{i=1}^{3}\pi(\mathbf{M}_{\text{i}}), \quad (13)$$

where $\pi(\mathbf{M}_{\text{i}})$, $\pi(\mathbf{C}_{\text{HHb}})$ and $\pi(\mathbf{C}_{\text{HbO2}})$ are the prior distributions of the respective unknown variables.

In reality, the absolute concentrations of oxy- and deoxyhemoglobin are not independent and depend on the total blood volume at a specific voxel. The blood volume at every voxel can vary and is typically unknown. Since the normalized spectra are used in the inversion and the normalization is performed per-spectrum, the potential quantitative information on the total blood volume is lost and the concentrations found are relative rather than absolute. Therefore, the only constraint imposed on the relative coefficients of oxy- and deoxyhemoglobin is that they cannot be negative, $\pi(\mathbf{C}_{\text{HHb}})$ can be modeled using the uniform pseudo-distribution

$$\pi(\mathbf{C}_{\text{HHb}}) = \prod_{\mathbf{r}\in\mathbf{G}}\pi\left(c'^{(\mathbf{r})}_{HHb}\right) = \begin{cases} 0, & \exists \mathbf{r} : c'^{(\mathbf{r})}_{HHb} < 0, \\ \delta, & \forall \mathbf{r} : c'^{(\mathbf{r})}_{HHb} \geq 0, \end{cases} \quad (14)$$

and $\pi(\mathbf{C}_{\text{HbO2}})$ can be defined analogously, where δ is a constant. Computationally Eq. 14 is implemented using appropriate inequality constraints.

When modelling the prior distributions of $\mathbf{M}_1$, $\mathbf{M}_2$ and $\mathbf{M}_3$ it is important to take into account the spatial dependencies of parameter values [8]. To achieve this, probabilistic graphical models are used to model the spatial variation of $\mathbf{M}_1$, $\mathbf{M}_2$ and $\mathbf{M}_3$ across neighboring grid points on the graph $(\mathbf{G}_n, \mathbf{G}_e)$, which corresponds to the grid $\mathbf{G}$. $\mathbf{G}_n$ is the set of pixels in the grid (graph nodes) and $\mathbf{G}_e$ is the set of spatial connections between the pixels (graph edges). Fig. 1a shows an example of a radial grid $\mathbf{G}$ of $n_{\text{ln}} = 5$ lines (white radial lines), each consisting of $n_{\text{pt}} = 3$ points, superimposed on a simulated OA image. The pixels used in inversion are marked in red and represent $\mathbf{G}_n$.

For $\mathbf{M}_1$ and $\mathbf{M}_3$, the values of the parameters do not depend directly on the values of neighboring nodes. Instead, due to the nature of light propagation, the spatial smoothness of the solution should be ensured globally [8]. Thus, an undirected graphical model, namely pairwise Markov random field [26], is used, with a Gibbs distribution, which takes the form $\pi(\mathbf{M}_{\text{i}}) = (1/Z)\exp\left(-\sum_{\mathbf{s}\in\mathbf{G}_n} V_i(\mathbf{s})\right), i = 1,3$ [27]. Here Z is a normalization constant and V_i is the potential function. Fig. 1b presents an undirected graph corresponding to the grid shown in Fig. 1a used to model the prior distributions of $\mathbf{M}_1$ and $\mathbf{M}_3$. The white lines connecting the graph nodes represent the graph edges $\mathbf{G_e}$. The common choice for the prior model is a Gaussian Markov Random Field [27]. For $\mathbf{M}_1$, the potential function V takes the following form:

$$\begin{aligned} V_1(\mathbf{s}) &= GMRF_1(\mathbf{s}), \\ GMRF_1(\mathbf{s}) &= \sum_{\mathbf{r}\in\partial\mathbf{s}} a_1^{(\mathbf{r},\mathbf{s})}\left|\mathbf{M}_1^{(\mathbf{s})} - \mathbf{M}_1^{(\mathbf{r})}\right|^2, \end{aligned} \quad (15)$$

where $\partial\mathbf{s}$ denotes the set of all neighbors of the node $\mathbf{s}$, and $a_1^{(\mathbf{r},\mathbf{s})}$ is a constant coefficient.

It has also been shown previously that for the nodes close to the surface, the correct values of $\mathbf{M}_1$ and $\mathbf{M}_3$ are more likely to lie close to the prior estimates $\hat{\mathbf{M}}_1^{(\mathbf{s})}$ and $\hat{\mathbf{M}}_3^{(\mathbf{s})}$ [8] . With tissue depth, this probability decreases. The constraints based on this observation proved essential for inversion stability. To reflect this behavior in a probability distribution, we augmented the potential functions as follows:

$$\begin{aligned} V_1(\mathbf{s}) &= GMRF_1(\mathbf{s}) + GG_1(\mathbf{s}), \\ GG_1(\mathbf{s}) &= \left(\frac{\left|\mathbf{M}_1^{(\mathbf{s})} - \mu_{m1}^{(\mathbf{s})}\right|}{2\sigma_{m1}^{(\mathbf{s})}}\right)^q, \end{aligned} \quad (16)$$

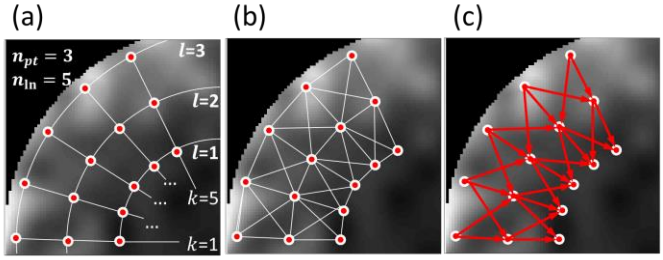

Fig. 1: BeMSOT inversion grid and corresponding graphical models. (a) A radial grid $\mathbf{G}$ (red dots) of $n_{\text{ln}} = 5$ lines (white radial lines), each consisting of $n_{\text{pt}} = 3$ points superimposed on a simulated OA image. (b) An undirected graph corresponding to $\mathbf{G}$ used to model the prior distributions of $\mathbf{M}_1$ and $\mathbf{M}_3$. (c) A directed graph corresponding to $\mathbf{G}$ used to model the prior distributions of $\mathbf{M}_2$ and to ensure that $\mathbf{M}_2$ decreases with depth.

For $\mathbf{M}_3$ the potential function $V_3(\mathbf{s})$ is defined analogously. $GG_i, i=1,3$ corresponds to the exponential part of a generalized Gaussian distribution parametrized by the shape parameter q and the scale parameters $\sigma_{m1}^{(\mathbf{s})}$ and $\sigma_{m3}^{(\mathbf{s})}$ [28, 29]. These scale parameters define ranges around the mean values $\mu_{m1}^{(\mathbf{s})}$ and $\mu_{m3}^{(\mathbf{s})}$ within which the values of $\mathbf{M}_1^{(\mathbf{s})}$ and $\mathbf{M}_3^{(\mathbf{s})}$ are more likely to lie. We will refer to these scale parameters as *deviations*. The mean values $\mu_{m1}^{(\mathbf{s})}$ and $\mu_{m3}^{(\mathbf{s})}$ are computed for each eigenfluence parameter $\mathbf{M}_i^{(\mathbf{s})}, i=1,3$ based on the prior estimates $\hat{\mathbf{M}}_1^{(\mathbf{s})}$ and $\hat{\mathbf{M}}_3^{(\mathbf{s})}$, as described [8]. It is important to note that the value of q is unknown at this point and remains to be defined.

While $\mathbf{M}_1$ and $\mathbf{M}_3$, do not have a clear relation to a single physical parameter but rather depend on both sO_2 and tissue depth, $\mathbf{M}_2$ has been shown to correlate primarily with tissue depth [8]. Therefore the constraints imposed on this parameter in the inversion are different from those imposed on $\mathbf{M}_1$ and $\mathbf{M}_3$. In contrast to the undirected graphical approach, a directed graphical model is used to model the spatial behavior of $\mathbf{M}_2$ and constrain it to decrease with depth. Fig. 1c presents a directed graph corresponding to the grid in Fig. 1a that is used to model the prior distributions of $\mathbf{M}_2$. The distribution of $\mathbf{M}_2^{(\mathbf{s})}$ at each node $\mathbf{s}$ is conditional on the values $\mathbf{M}_2^{(\mathbf{S})}$ of the parent nodes $\mathbf{S}$ and is modeled as a uniform distribution in the range between $\min \mathbf{M}_2^{(\mathbf{S})}$ and MIN_2 through application of appropriate linear constraints.

Substituting Eqs. 9, 12-14 and 16 into Eq. 10 and taking into account the inequalities modeling the distribution of $\mathbf{M}_2$, $\mathbf{C}_{\mathrm{HHb}}$ and $\mathbf{C}_{\mathrm{HbO2}}$ yields

$$\begin{aligned}\boldsymbol{\Theta}_{\mathbf{MAP}} &= \arg\min_{\boldsymbol{\Theta}} \left\| \mathbf{P}'_{\mathrm{measured}} - \mathbf{P}_{\mathbf{model}}(\boldsymbol{\Theta}) \right\|_{\boldsymbol{\Sigma}_\alpha}^2 \\ &+ \beta \sum_{\mathbf{s}\in\mathbf{G_N}} \left[\left(\sum_{\mathbf{r}\in\partial\mathbf{s}} a_1^{(\mathbf{r},\mathbf{s})} \left| \mathbf{M}_1^{(\mathbf{s})} - \mathbf{M}_1^{(\mathbf{r})} \right|^2 + a_3^{(\mathbf{r},\mathbf{s})} \left| \mathbf{M}_3^{(\mathbf{s})} - \mathbf{M}_3^{(\mathbf{r})} \right|^2 \right) \right. \\ &\left. + \left(\frac{\left| \mathbf{M}_1^{(\mathbf{s})} - \mu_{m1}^{(\mathbf{s})} \right|}{2\sigma_{m1}^{(\mathbf{s})}} \right)^q + \left(\frac{\left| \mathbf{M}_3^{(\mathbf{s})} - \mu_{m3}^{(\mathbf{s})} \right|}{2\sigma_{m3}^{(\mathbf{s})}} \right)^q \right], \end{aligned} \tag{17}$$

$$\begin{aligned} &\text{subject to}: \\ &\mathbf{M}_2^{(k,l)} > \mathbf{M}_2^{(k+1,l)}, \\ &\mathbf{M}_2^{(k,l)} > \mathbf{M}_2^{(k+1,l+1)}, \\ &\mathbf{M}_2^{(k,l)} > \mathbf{M}_2^{(k+1,l-1)} \\ &\mathbf{C}_{\mathrm{HHb}}^{(k,l)} \geq 0, \mathbf{C}_{\mathrm{HbO2}}^{(k,l)} \geq 0. \end{aligned}$$

In Eq. 17 β is a constant; $\boldsymbol{\Sigma}_\alpha = \boldsymbol{\Sigma} + \alpha\mathbf{I}$, where $\mathbf{I}$ is the identity matrix; and α is the diagonal loading constant, which dampens large variations in $\boldsymbol{\Sigma}$ that may arise due to large variations in SNR across the measured spectra. Eq. 25 is the main equation of BeMSOT inversion. In order to solve it one needs to define values of the parameters q, $a_1^{(\mathbf{r},\mathbf{s})}$, $a_3^{(\mathbf{r},\mathbf{s})}$, $\sigma_{m1}^{(\mathbf{s})}$ and $\sigma_{m3}^{(\mathbf{s})}$, as well as estimate $\boldsymbol{\Sigma}$. The values for the parameters are set as described in the next subsection. Estimation of $\boldsymbol{\Sigma}$ is described in Sec. III-B. Eq. 17 is solved using the sequential quadratic programming (SQP) algorithm supplied in MATLAB.

A.4. Choosing Parameters of the Prior Distributions

The prior probabilities $\pi(\mathbf{M}_i), i=1,3$ incorporate prior knowledge about the deviation of model parameters from the prior estimates $\hat{\mathbf{M}}_1^{(k,l)}$ and $\hat{\mathbf{M}}_3^{(k,l)}$, which are computed as described previously [8]. The deviations $\sigma_{m1}^{(k,l)}$ and $\sigma_{m3}^{(k,l)}$ of the generalized Gaussian distribution, which determine the deviation of the optimized eigenfluence parameters from $\mu_{m1}^{(k,l)}$ and $\mu_{m3}^{(k,l)}$, increase linearly with tissue depth because $\hat{\mathbf{M}}_1^{(k,l)}$ and $\hat{\mathbf{M}}_3^{(k,l)}$ become less accurate with depth [8]. Given the initial deviations $\sigma_{m1}^{(k,0)}$ and $\sigma_{m3}^{(k,0)}$ for the surface grid points, the deviations at an arbitrary grid point are defined as $\sigma_{m1}^{(k,l)} = \gamma_1(d)\cdot\sigma_{m1}^{(k,0)}$, $\sigma_{m3}^{(k,l)} = \gamma_3(d)\cdot\sigma_{m3}^{(k,0)}$, where γ_1 and γ_3 are coefficients that depend on the depth d of the considered point. The values of γ_1 and γ_3 in this study were retained as described [8], and the values of $\sigma_{m1}^{(k,0)}$ and $\sigma_{m1}^{(k,0)}$ were selected based on cross-validation using simulated IPR maps (see Supplementary Materials).

The coefficients that govern the spatial smoothness of $\mathbf{M}_1$ and $\mathbf{M}_3$ were set to be inversely proportional to the Euclidean distance $\|\mathbf{r}-\mathbf{s}\|_2$ between the neighboring pixels $\mathbf{r}$ and $\mathbf{s}$: $a_1^{(\mathbf{r},\mathbf{s})} = a_3^{(\mathbf{r},\mathbf{s})} = w\frac{1}{\|\mathbf{r}-\mathbf{s}\|_2}$.

The parameters of the Bayesian inversion method, namely q, w, $\sigma_{m1}^{(\mathbf{s})}$ and $\sigma_{m3}^{(\mathbf{s})}$, were selected using cross-validation of a set of simulations described in the following subsection; the selection process itself is described in Supplementary Materials.

B. Noise Estimation in BeMSOT Using a Spectral Reliability Map (SRM)

Since the level of noise in OA spectra depends on the voxel location, with shallower voxels typically showing better signal-to-noise ratio (SNR) than deeper ones, noise in eMSOT spectra needs to be estimated on a per-voxel (per-collected spectrum) basis. To estimate the noise present in each individual spectrum, we developed a model for normalized OA spectra, termed a *OA spectral model*. We use the OA spectral model to estimate the underlying ideal noise-free normalized OA spectra of experimental noisy normalized OA spectra, and then estimate the level of random noise in spectra obtained at different locations (voxels), giving rise to a spatial map of estimated noise variance. This map, which we term a *spectral reliability map* (SRM), is used to weight different spectra selected for the BeMSOT inversion according to the amount of estimated noise.

B.1. OA Spectral Model

The OA spectral model describes noise-free normalized OA spectra recorded at different locations within tissue. Spectrum location $\mathbf{r}$ is not important for model derivation and is therefore omitted to simplify the notation. Building on the eMSOT assumption that the spectrum of light fluence anywhere within tissue can be accurately modeled using a small set of base spectra, the OA spectral model assumes that all possible normalized OA spectra $p'(\lambda)$ (Eq. 1) can also be modelled as a linear combination of a few base spectra $p_i(\lambda)$. These spectra $p_i(\lambda)$ are derived from analysis of a training dataset of noise-free normalized OA spectral patterns. This dataset captures variations in normalized OA spectra due to fluence and absorption of hemoglobin. The training dataset was generated as follows:

1. A set $\hat{\mathbf{\Phi}} = \{\Phi_i(\lambda) \mid i = 1...70 \times 21\}$ of 1470 fluence spectra $\Phi_i(\lambda)$ was computed as a 1-D analytical solution for Eq. 2 in an infinite medium in which hemoglobin is the only absorber, as described for eMSOT [8]. The following parameters were assumed: $\mu_a = 0.3$ cm^{-1} at 800 nm, $\mu'_s =$ 10 cm^{-1}, depth of up to 1 cm with a step size of 0.0145 cm (70 in total) and for oxygenation levels of 0%-100% with a step size of 5% (21 in total).
2. Absorption spectra of hemoglobin at different oxygenation levels $\hat{\boldsymbol{\mu}}_a = \{\mu_{a,i} \mid i = 1...21\}$ were calculated. While absorption spectra can be calculated as $\mu_a = c'_{\mathrm{HHb}}\,\varepsilon_{\mathrm{HHb}}(\lambda) + c'_{\mathrm{HbO2}}\,\varepsilon_{\mathrm{HbO2}}(\lambda)$, we did not use this approach because we are interested only in the shape of the absorption spectrum, not absolute absorption values. Therefore we computed absorption spectra as a function of tissue oxygen saturation c_{O2}: $\mu_a = c_{\mathrm{O2}}\varepsilon_{\mathrm{HHb}}(\lambda) + (1 - c_{\mathrm{O2}})\varepsilon_{\mathrm{HbO2}}(\lambda)$. We varied c_{O2} from 0% to 100% with a step size of 5%, producing a total of 21 absorption spectra of hemoglobin.
3. Each fluence spectrum in $\hat{\mathbf{\Phi}}$ obtained in step 1 was multiplied element-wise by every absorption spectrum in $\hat{\boldsymbol{\mu}}_a$ calculated in step 2. The resulting spectral patterns were normalized to their respective l_2-norms, producing a training dataset $\hat{\mathbf{P}}'$ of 21×1470 normalized OA spectra (30,870).

PCA was applied to this training dataset $\hat{\mathbf{P}}'$ to derive the base spectra $p_i(\lambda)$ as follows:

1. Since PCA requires that input data have a mean value of zero, the mean normalized OA spectrum $p_{\mathrm{M}}(\lambda) = \mathrm{mean}(\hat{\mathbf{P}}')$ was computed from the training set $\hat{\mathbf{P}}'$ and subtracted from every spectrum in $\hat{\mathbf{P}}'$, resulting in a zero-mean input set $\hat{\mathbf{P}}'_0$ of 30,870 spectra.
2. PCA was applied to the input set $\hat{\mathbf{P}}'_0$ of spectral patterns obtained in step 1. The resulting principal components were the base spectra $p_i(\lambda)$.

These base spectra (principal components) derived from a distinct precomputed set $\hat{\mathbf{P}}'_0$ can now be combined linearly with the mean spectrum of the training dataset $p_{\mathrm{M}}(\lambda)$ to model an arbitrary normalized OA spectrum $p'(\mathbf{r},\lambda)$ from a specific location $\mathbf{r}$ in an OA dataset:

$$p'(\mathbf{r},\lambda) = p_{\mathrm{M}}(\lambda) + \sum_{i=1}^{D} a_{\mathrm{i}}(\mathbf{r})\, p_{\mathrm{i}}(\lambda), \tag{18}$$

where $a_{\mathrm{i}}(\mathbf{r}) = \left\langle \mathbf{p}' - \mathbf{p}_{\mathrm{M}}, \mathbf{p}_i \right\rangle_{\lambda}$, with $\langle .,. \rangle_{\lambda}$ denoting the scalar product of spectra. The number of components D returned by PCA is equal to the number of wavelengths used (21 in this study). Only a subset of these base spectra is typically needed to approximate the data sufficiently well, i.e.

$$\{\mathbf{p}_{\mathrm{M}}, \mathbf{p}_i \mid i = 1...D_{\mathrm{m}}\}, \tag{19}$$

where $D_{\mathrm{m}} < D$. Eq. 13 will be referred to as a D_{m}-dimensional OA spectral model.

B.2. Spectral Reliability Map (SRM)

Next we applied the D_{m}-dimensional OA spectral model to noisy OA spectra to estimate what the ideal, noise-free measurements should be. The difference between the noise-free estimation and the experimental values provides an estimate of the noise in the experimental spectra. We modeled a noisy experimental normalized OA spectrum $p'_{\mathrm{exp}}(\mathbf{r},\lambda)$ as $p'_{\mathrm{exp}}(\mathbf{r},\lambda) = p_{\mathrm{nf}}(\mathbf{r},\lambda) + n(\mathbf{r},\lambda)$, where $p_{\mathrm{nf}}(\mathbf{r},\lambda)$ is a noise-free spectrum of initial pressure and $n(\mathbf{r},\lambda)$ is noise. Since the main source of OA noise is electronic noise in the imaging system [9], we modeled $n(\mathbf{r},\lambda)$ as a random Gaussian process with zero mean, assuming that variance of $n(\mathbf{r},\lambda)$ is constant at all wavelengths, but might vary with $\mathbf{r}$. Since $p_{\mathrm{nf}}(\mathbf{r},\lambda)$ lies almost entirely in a subspace of spectra defined by the D_{m} base spectra $p_i(\lambda)$ and since $n(\mathbf{r},\lambda)$ is random and therefore equally distributed across all base spectra, an estimate p_{est} of the noise-free spectrum can be obtained as:

$$\mathbf{p}_{\mathrm{est}} = \mathbf{p}_{\mathrm{M}} + \sum_{i=1}^{\dim_{\mathrm{NIPS}}} \left\langle \mathbf{p}'_{\mathrm{exp}} - \mathbf{p}_{\mathrm{M}}, \mathbf{p}_i \right\rangle_{\lambda} \mathbf{p}_i. \tag{20}$$

Estimation of noise n_{est} can then be calculated as

$$n_{\mathrm{est}}(\mathbf{r},\lambda) = p_{\mathrm{exp}}(\mathbf{r},\lambda) - p_{\mathrm{est}}(\mathbf{r},\lambda). \tag{21}$$

This is equivalent to projecting $\mathbf{p}'_{\mathrm{exp}} - \mathbf{p}_{\mathrm{M}}$ onto the last $D - D_{\mathrm{m}}$ base spectra. Given an MSOT dataset $p(\mathbf{r},\lambda)$, Eqs. 20 and 21 can be applied to normalized OA spectra $\mathbf{p}'(\mathbf{r})$ at every pixel location $\mathbf{r}$ to estimate the noise $\mathbf{n}_{\mathrm{est}}(\mathbf{r})$ superimposed onto the measurements. The corresponding variance in the noise $Var(\mathbf{n}_{est}(\mathbf{r}))$ can be calculated and spatially mapped, giving what we term a *spectral reliability map (SRM)*:

$$SRM(\mathbf{r}) = Var(\mathbf{n}_{est}(\mathbf{r})). \quad (22)$$

The SRM can then be used to weight spectra chosen for eMSOT inversion such that noisier measured normalized OA spectra will influence BeMSOT inversion less.

C. Validation and Performance Assessment

In order to select optimal dimensionality D_{m} of the OA spectral model and to define values of the parameters of prior distributions, simulations of multispectral IPR maps were used. To assess the performance of BeMSOT, simulations were created with spatially varying amounts of noise. For such simulations with inhomogeneous noise distribution, IPR maps were simulated first, for which the corresponding transducer signals were calculated. Noise was added to the transducer signals and MSOT images were reconstructed from the noisy signals. MSOT images created from multispectral IPR maps were used for BeMSOT inversion.

C.1. Simulations of IPR maps

Multispectral IPR maps of a circular tissue sample (radius, 1 cm) with randomly varying optical properties were simulated as described [8] for different excitation wavelengths. Fig. 2 shows the simulated maps, which were generated in the following manner:

1. Spatial maps of optical absorption ($\mu_a(\mathbf{r})$) and reduced scattering ($\mu'_s(\mathbf{r})$) coefficients were created for an illumination wavelength of 800 nm, which is the isosbestic point of hemoglobin. Fig. 2a-b shows an example of random spatial maps of optical properties, while Table 1 provides the means and standard deviations of the normal distributions used. Random maps of tissue sO_2 were created by assuming a normal distribution of sO_2 values. Fig. 2c shows an example of a simulated sO_2 map.
2. Using the maps specified in step 1 as well as the absorption spectra of oxy- and deoxyhemoglobin, the optical absorption $\mu_a(\mathbf{r},\lambda)$ was constructed for the entire wavelength range used (700-900 nm, step size of 10 nm, 21 maps in total).
3. The *optical forward problem* was solved using finite-element solution to the diffusion equation (Eq. 2) to simulate light propagation through the sample, generating a light fluence map $\Phi(\mathbf{r},\lambda)$ for all illumination wavelengths.
4. According to Eq. 1, the multiplication of the absorption map $\mu_a(\mathbf{r},\lambda)$ specified in step 2 and the light fluence map $\Phi(\mathbf{r},\lambda)$ obtained in step 3 gives the simulated IPR map $p(\mathbf{r},\lambda)$. This map assumes that $\Gamma(\mathbf{r})=1$, which does not affect sO_2 quantification accuracy because all spectra $\mathbf{p}(\mathbf{r})$ are normalized in eMSOT and BeMSOT. Fig. 2d presents a simulated IPR map that corresponds to the optical properties defined in Fig. 2a-c.

IPR maps were generated with different distributions of optical properties in order to simulate a reasonable range of tissue heterogeneity created by the presence of tissue structures.

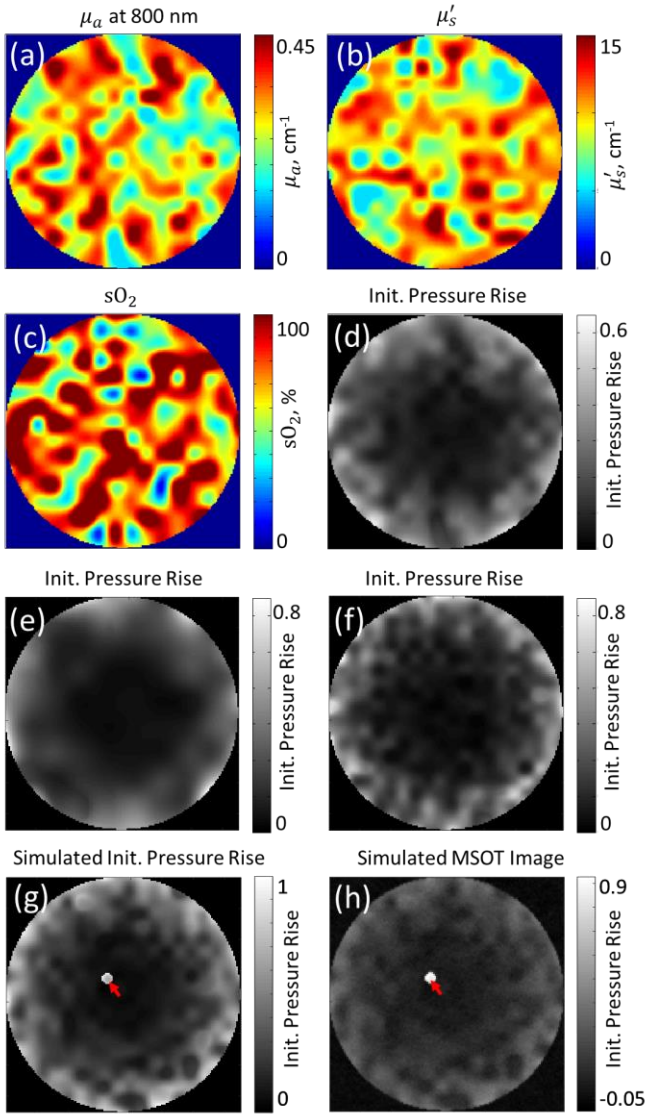

Fig. 2: Simulations of IPR maps and MSOT images. (a-c) Maps generated for an illumination wavelength of 800 nm based on randomly generated values of (a) μ_a, (b) μ'_s and (c) sO_2. (d) IPR image simulated from the maps in panels (a)-(c); (e,f) IPR maps simulated with (e) low and (f) high heterogeneity in the distributions of optical properties. (g) IPR image simulated with an absorbing vessel in deep tissue (red arrow). (h) Simulated MSOT image corresponding to the IPR map shown in panel (e) and showing the simulated blood vessel (red arrow). Negative values in panel (h) are an artifact of reconstruction.

TABLE 1. Simulation specifications.

Purpose	μ_a mean, cm^{-1}	μ_a std, cm^{-1}	μ'_s mean, cm^{-1}	μ'_s std, cm^{-1}	sO_2 mean, %	sO_2 std, %	Number of simulations
Optimization of the NF-NIPS model and SRM (Fig. 3)	0.07; 0.1; 0.15; 0.2; 0.25; 0.3	0.1	10	3	5-95, step of 5	20; 30	1710
Application of BeMSOT to simulations of MSOT images (Fig. 5)	0.3	0.1	10	3	5-95, step of 5	20; 30	285
Optimization of BeMSOT (Suppl. Fig. 1)	0.1; 0.2; 0.3	0.1	10	3	5-95, step of 5	20; 30	171

Fig. 2e shows an example of a simulation with low heterogeneity; Fig. 2f, an example with high heterogeneity.

Since the SRM is evaluated on a per-pixel level, the individual spectra extracted from the IPR simulations were augmented with zero-mean Gaussian nose $\mathbf{n}$ of the following powers: 0.8, 1.5, 2.5, 4.5, 6, 8 or 10 percent of spectra power (referred to as percent noise).

C.2. Simulations of MSOT images

To create simulations with heterogeneous noise distribution, we started from the simulated IPR maps and solved the *acoustic forward problem* using a linear model of pressure wave propagation [30, 31], obtaining the corresponding OA pressure signals recorded by the piezoelectric transducers of the imaging system. Then zero-mean Gaussian noise was added to the simulated transducer signals, which were reconstructed into MSOT images. This process involved the following steps:

1. An IPR map $\mathbf{P}_\lambda$ for a specific illumination wavelength λ was simulated and reshaped into a vector $\mathbf{p}_\lambda$.
2. The *forward acoustic problem* was solved. The corresponding OA pressure signals $\mathbf{s}_{\text{pr}}$ were simulated as $\mathbf{s}_{\text{pr}} = \mathbf{A}_c\mathbf{p}_\lambda$, where $\mathbf{A}_c$ is a model matrix representing the linear model of OA wave propagation. The detection geometry represented in $\mathbf{A}_c$ assumed the geometry of a commercially available, limited-view 2D MSOT imaging system [32], comprising 256 detectors arranged in a ring with a radius of 4 cm, which provides angular coverage of 270 degrees.
3. Zero-mean Gaussian noise was superimposed upon the simulated signals $\mathbf{s}_{\text{pr}}$ to obtain noisy signals $\mathbf{s}_{\text{ns}}$.
4. The *inverse acoustic problem* was then solved by using the noisy signals $\mathbf{s}_{\text{ns}}$ along with $\mathbf{A}_c$ in a model-based reconstruction algorithm [30, 31] to obtain the distorted IPR image $\mathbf{P}_{\text{rec}}$. In all cases, speed of sound was assumed to be 1,530 $\text{m}\cdot\text{s}^{-1}$ during signal simulation and reconstruction. Since noise is superimposed on the signals (step 3) rather than on the spectra, the noise in $\mathbf{P}_{\text{rec}}$ is non-uniformly distributed in space, with SNR varying directly with signal intensity.

For example, the simulated IPR map in Fig. 2g was reconstructed into the noisy MSOT image $\mathbf{P}_{\text{rec}}$ in Fig. 2h. The reconstructed image contains negative values, which are a reconstruction artifact [33]. The red arrow marks the location of a simulated blood vessel, which should have a much higher SNR than the surrounding area.

For each simulated IPR dataset, the power of noise was varied so that the mean peak SNR (PSNR) of the reconstructed datasets varied from 36 to 32 dB in 1-dB steps. PSNR was defined as $PSNR = 10\log_{10}\frac{\left(\max \mathbf{P}_{\text{rec}}\right)^2}{MSE\left(\mathbf{P}_{\text{rec}},\mathbf{P}_\lambda\right)}$, with $MSE\left(\mathbf{P}_{\text{rec}},\mathbf{P}_\lambda\right)$ denoting the mean squared error of the reconstructed image.

C.3. Performance evaluation of the OA spectral model, SRM and BeMSOT

For each simulated noise-free normalized OA spectrum $\mathbf{p}'_{\text{nf}}$, the fitting residual $res = \left\|\mathbf{p}'_{\text{nf}} - \mathbf{p}_{\text{est}}\right\|_2$ was computed, where $\mathbf{p}_{\text{est}}$ was obtained using the normalized OA model according to Eq. 14. The fitting residual was computed for all test spectra for different OA spectral model dimensionalities D_{m}. For a particular value of D_{m}, lower residual values mean better approximation by the dim_{NIPS}-dimensional OA spectral model. For every simulated noisy normalized OA spectrum $\mathbf{p}'_{\text{exp}}$, the superimposed noise was estimated using Eqs. 20 and 21. The variance $Var\left(\mathbf{n}_{est}(\mathbf{r})\right)$ was compared to the actual variance $Var\left(\mathbf{n}(\mathbf{r})\right)$ of superimposed noise. For a particular value of D_{m}, lower relative estimation errors (i.e. $\frac{\left|Var\left(\mathbf{n}_{est}(\mathbf{r})\right) - Var\left(\mathbf{n}(\mathbf{r})\right)\right|}{Var\left(\mathbf{n}(\mathbf{r})\right)}\cdot 100\%$) mean better noise estimation by the D_{m}-dimensional OA spectral model.

BeMSOT performance was compared to that of eMSOT and linear unmixing based on mean absolute sO_2 estimation error in a deep-seated blood vessel (representative of a target feature in the sample), as well as in non-vessel areas covered by the grid $\mathbf{G}$ used for inversion (representative of sample background). For every pixel, the absolute sO_2 estimation error was computed as $\left|sO2_{a\text{lg}} - sO2_{GS}\right|$, where $sO2_{a\text{lg}}$ is the sO_2 value obtained by a certain algorithm and $sO2_{GS}$ is the gold standard value.

In all cases, sO_2 level in the blood vessel was set to be 25% higher than the level in the background, or to 100% if the mean sO_2 level of the background was above 75%. For example, if sO_2 of the background was 35%, sO_2 level of the vessel was set to 60% (35+25%); if sO_2 of the background was 80%, sO_2 level of the vessel was set to 100%.

IV. Results

A. Noise estimation using the OA spectral model and SRM

Fig. 3 demonstrates the optimization of the OA spectral model and the noise estimation capability of the SRM based on analysis of 384,750 simulated normalized OA spectra sparsely sampled from 1,710 IPR simulations (225 spectra per simulated dataset). Fig. 3a shows how the fitting residual varies with dimensionality D_{m}; most of the signal is accounted for by the first four principal components. Fig. 3b shows a reasonable fit between the SRM-estimated variance in noise based on a four-dimensional OA spectral model and the ideal prediction of a 1:1 correspondence (orange line). Finally, Fig. 3c shows that D_{m} values of 3 or 4 minimize relative error in the estimation of the variance of noise. Using more than 4 components leads to model overfitting and increases estimation error due to noise being interpreted as signal. Therefore, subsequent computations were carried out using a four-dimensional OA spectral model.
Fig. 3d presents a simulated IPR dataset (one wavelength shown) in which zero-mean Gaussian noise was added to the spectra at four energies. Fig. 3e shows the corresponding SRM

based on Eq. 21 and $D_{\mathrm{m}} = 4$. The spatial analysis of variance identifies areas with different SNR.

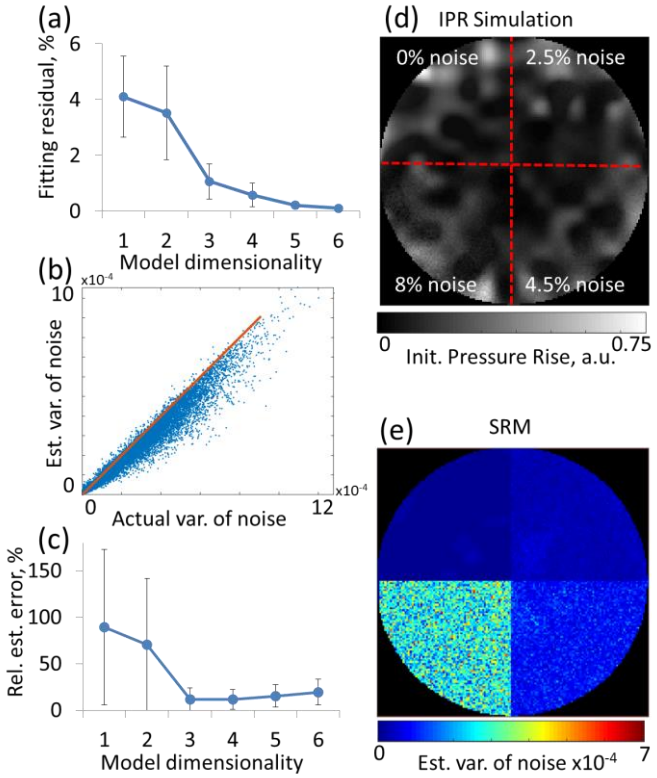

Fig. 3: Optimization and performance of the OA spectral model and SRM. (a) Dependence of fitting residuals res on dimensionality D_{m} of the normalized OA spectral model for approximating noise-free spectra. Mean data (dots) are shown with standard deviations (error bars). (b) Variance of noise estimated with a four-dimensional normalized OA spectral model plotted against the actual standard deviation of noise. The orange line shows ideal 1-to-1 correspondence. (c) Relative errors in the estimation of variance of noise produced by the normalized OA spectral model depending on its dimensionality. Mean data (dots) are shown with standard deviation (error bars). (d) A simulated IPR map (one wavelength presented) with zero-mean Gaussian noise of the specified energy (as noise %) superimposed onto the simulated spectra in four sectors. (e) An SRM computed for the simulated data shown in panel (d).

B. Comparison of eMSOT and BeMSOT

BeMSOT and conventional eMSOT were compared in their ability to estimate sO_2 from a deep-seated blood vessel and background areas of the image. The results were compared with those obtained by standard linear mixing as a reference. Simulated MSOT images with mean PSNR of 33 and 36 dB in the reconstructed data were used in order to showcase the performance of each algorithm. Fig. 4a presents the simulated MSOT image obtained for illumination at 900 nm, and spectra sampled from three image locations (Fig. 4b-d). SNR varies over the image, with less noise in highly absorbing and shallower areas. Fig. 4e-h show the error of BeMSOT and eMSOT in estimating sO_2 in the deep-seated vessel. As expected, BeMSOT is better able to estimate sO_2 than eMSOT when the target is surrounded by spectra of significantly lower quality, and this is true at both PSNRs tested.

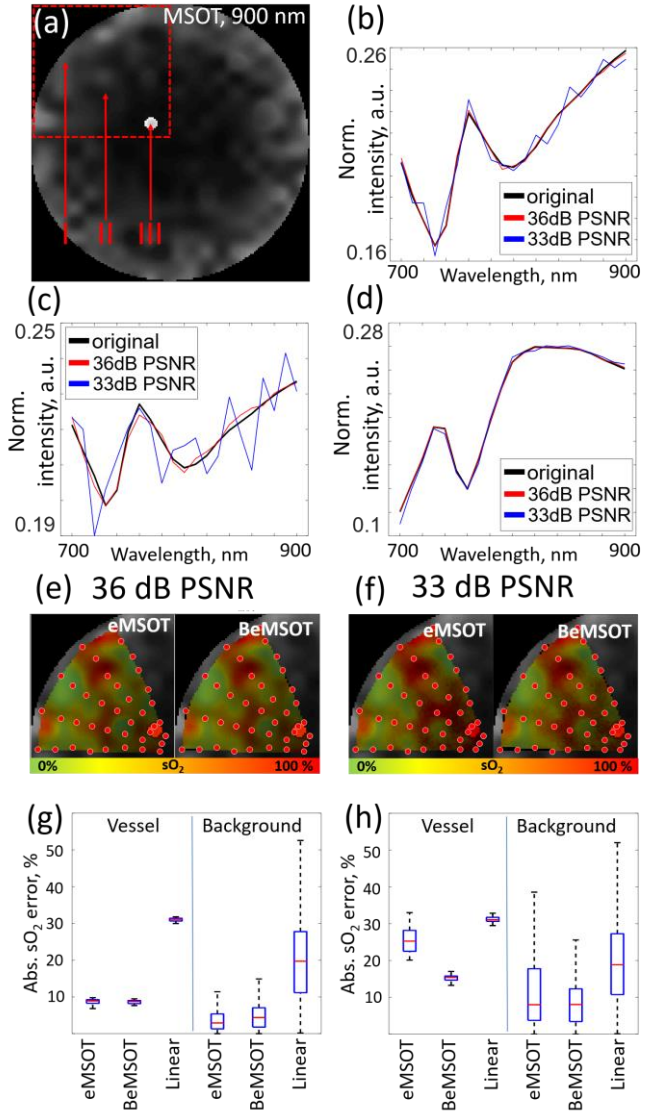

Fig. 4: Comparison of BeMSOT and eMSOT for quantifying sO_2 in simulated MSOT images. (a) A map of simulated IPR (one wavelength presented). The red dashed square marks the ROI shown in panels (e) and (f), while I, II and III denote locations of the spectra shown in panels (b)-(d). (b-d) Respective spectra from locations I-III in panel (a). Black lines correspond to original spectra; red lines, reconstructed data with mean PSNR of 36; and blue lines, reconstructed data with mean PSNR of 33 dB. (e,f) Values for sO_2 obtained from the reconstructions with mean PSNR of (e) 36 dB or (f) 33 dB, overlaid on the IPR image. Inversion grids are shown with red circles (active pixels) and blue circles (inactive pixels). Blue pixels were excluded from the inversion because the corresponding spectra had negative values. (g,h) Errors in sO_2 estimation for the vessel and background obtained with BeMSOT, eMSOT or linear unmixing for the reconstructions with mean PSNR of (g) 36 dB or (h) 33 dB. Blue boxes indicate first and third quartiles; red lines, medians; and whiskers, 2.7 standard deviations from the mean.

These results were confirmed in statistical analysis of 285 simulations (Fig. 5). Whereas eMSOT performance degrades with increasing noise, BeMSOT can recover sO_2 of the vessel more accurately even at low SNRs. Both methods, in contrast,

perform similarly well for the background ROI, indicating that BeMSOT offers advantages over eMSOT primarily in image areas with strong SNR heterogeneity.

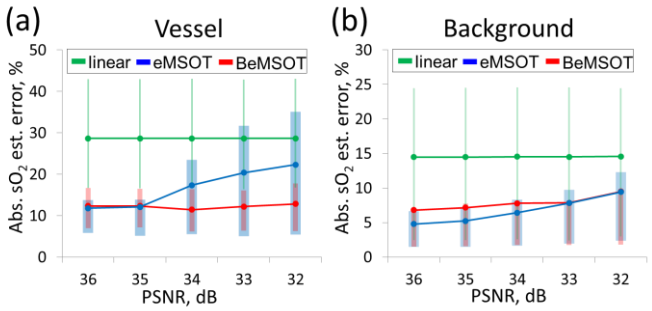

Fig. 5: Statistical evaluation of BeMSOT performance in simulations of MSOT images. Mean error in sO_2 estimation by BeMSOT (red line), eMSOT (blue line) and linear unmixing (green line) in (a) target vessel and (b) background as a function of mean PSNR of the reconstructed images. Results are based on 285 simulations of MSOT images. Error bars indicate first and third quartiles of the plotted data.

An example comparison of eMSOT and BeMSOT in experimental images of tissue mimicking phantoms can be found in Supplementary Materials (Suppl. Fig. 2).

V. Discussion and Conclusion

The mathematical framework of Bayesian inversion has been used extensively for the development of methods that offer robust solutions in inverse problems related to image reconstruction [27, 34], in particular in the field of optoacoustic imaging [12, 14]. In this work, we propose a Bayesian method for the inversion of the eigenspectra model to quantitatively estimate sO_2 level accurately in OA data with spatially heterogeneous noise.

To enable Bayesian formulation of the eMSOT inverse problem, we developed a novel tool called the SRM to estimate noise in the OA spectra. The SRM supports two functions: (1) to estimate the covariance of noise, which allows spectra to be weighted automatically based on their reliability; and (2) to identify well-reconstructed parts of the image for analysis. Even if unreliable areas are included in the BeMSOT inversion, the corresponding SRM can be used as an indication of the trustworthiness of the results. The proposed Bayesian inversion method can flexibly rely more on the less noisy measurements and suppress the impact of noisy data, therefore enhancing the accuracy of sO_2 estimation in data with spatially varying SNR.

Such spatial variation of noise power is characteristic of MSOT. Since MSOT image formation involves light absorption, the images are influenced by heterogeneous noise. Superficial regions as well as highly absorbing structures such as blood vessels show high intensity in images and so provide high SNR, while deeper and less-absorbing areas produce weaker signal easily dominated by noise.

Formulation of the inversion algorithm in Bayesian terms also allows studying how different parameters and constraints, such as constraints of the search space or smoothness of the solution, influence the overall performance of the method and interpretation of the results in probabilistic terms. This comes at the cost of speed: inversion typically takes ~60 sec for BeMSOT but only ~5 sec for eMSOT.

Since the presence of prominent absorbers other than oxy- and deoxyhemoglobin violates the assumptions of the eigenspectra model, in future work, the SRM may be adapted to take into account other absorbers, either separately from BeMSOT or in conjunction with an appropriately adapted BeMSOT algorithm. Optical wavelength selection, similarly to linear unmixing [35], may also improve sO_2 estimation accuracy by BeMSOT. Future studies could try to improve inversion accuracy and speed using neural networks, which show promise for applications to the inverse problems in quantitative optoacoustics [36, 37].

We have presented a novel Bayesian method for sO_2 quantification from MSOT images as well as a method to estimate noise present in the measured OA spectra. It is possible that the extension of this method that takes into account absorbers other than hemoglobin may be useful for quantifying other parameters useful to basic biology and disease, which may substantially extend and improve the quantitative potential of MSOT.

Acknowledgment

We thank A. Chapin Rodríguez, PhD for helpful suggestions on the manuscript.

References

1. Vaupel, P. and L. Harrison, *Tumor hypoxia: causative factors, compensatory mechanisms, and cellular response.* The oncologist, 2004. **9**(Supplement 5): p. 4-9.
2. Logothetis, N.K. and B.A. Wandell, *Interpreting the BOLD signal.* Annu. Rev. Physiol., 2004. **66**: p. 735-769.
3. Ntziachristos, V., *Going deeper than microscopy: the optical imaging frontier in biology.* Nat Methods, 2010. **7**(8): p. 603-14.
4. Mohajerani, P., et al., *Optical and optoacoustic model-based tomography: theory and current challenges for deep tissue imaging of optical contrast.* IEEE Signal Processing Magazine, 2015. **32**(1): p. 88-100.
5. Cox, B., et al., *Quantitative spectroscopic photoacoustic imaging: a review.* J Biomed Opt, 2012. **17**(6): p. 061202.
6. Cox, B., J. Laufer, and P. Beard. *The challenges for quantitative photoacoustic imaging*. in *SPIE BiOS: Biomedical Optics*. 2009. International Society for Optics and Photonics.
7. Maslov, K., H.F. Zhang, and L.V. Wang, *Effects of wavelength-dependent fluence attenuation on the noninvasive photoacoustic imaging of hemoglobin oxygen saturation in subcutaneous vasculature in vivo.* Inverse Problems, 2007. **23**(6): p. S113.
8. Tzoumas, S., et al., *Eigenspectra optoacoustic tomography achieves quantitative blood oxygenation imaging deep in tissues.* Nature Communications, 2016. **7**: p. 12121.
9. Tzoumas, S., et al., *Spatiospectral denoising framework for multispectral optoacoustic imaging based on sparse signal representation.* Medical physics, 2014. **41**(11): p. 113301.
10. Wang, L.V. and H.-i. Wu, *Biomedical optics: principles and imaging*. 2012: John Wiley & Sons.
11. Tarvainen, T., et al., *Reconstructing absorption and scattering distributions in quantitative photoacoustic tomography.* Inverse Problems, 2012. **28**(8): p. 084009.
12. Tarvainen, T., et al., *Bayesian image reconstruction in quantitative photoacoustic tomography.* IEEE transactions on medical imaging, 2013. **32**(12): p. 2287-2298.
13. Pulkkinen, A., et al., *A Bayesian approach to spectral quantitative photoacoustic tomography.* Inverse Problems, 2014. **30**(6): p. 065012.
14. Pulkkinena, A., et al. *Bayesian parameter estimation in spectral quantitative photoacoustic tomography*. in *Proc. of SPIE Vol*. 2016.

15. Cox, B., S. Arridge, and P. Beard, *Estimating chromophore distributions from multiwavelength photoacoustic images.* JOSA A, 2009. **26**(2): p. 443-455.
16. Cox, B.T., et al., *Two-dimensional quantitative photoacoustic image reconstruction of absorption distributions in scattering media by use of a simple iterative method.* Applied Optics, 2006. **45**(8): p. 1866-1875.
17. Banerjee, B., et al., *Quantitative photoacoustic tomography from boundary pressure measurements: noniterative recovery of optical absorption coefficient from the reconstructed absorbed energy map*. JOSA A, 2008. **25**(9): p. 2347-2356.
18. Yao, L., Y. Sun, and H. Jiang, *Quantitative photoacoustic tomography based on the radiative transfer equation.* Optics letters, 2009. **34**(12): p. 1765-1767.
19. Cox, B., T. Tarvainen, and S. Arridge, *Multiple illumination quantitative photoacoustic tomography using transport and diffusion models.* Tomography and Inverse Transport Theory, G. Bal, D. Finch, P. Kuchment, J. Schotland, P. Stefanov, and G. Uhlmann, eds, 2011. **559**: p. 1-12.
20. Bu, S., et al., *Model-based reconstruction integrated with fluence compensation for photoacoustic tomography.* IEEE Transactions on Biomedical Engineering, 2012. **59**(5): p. 1354-1363.
21. Mamonov, A.V. and K. Ren, *Quantitative photoacoustic imaging in radiative transport regime.* arXiv preprint arXiv:1207.4664, 2012.
22. Saratoon, T., et al., *A gradient-based method for quantitative photoacoustic tomography using the radiative transfer equation.* Inverse Problems, 2013. **29**(7): p. 075006.
23. Kaipio, J. and E. Somersalo, *Statistical and computational inverse problems*. Vol. 160. 2006: Springer Science & Business Media.
24. Calvetti, D. and E. Somersalo, *An Introduction to Bayesian Scientific Computing: Ten Lectures on Subjective Computing*. Vol. 2. 2007: Springer Science & Business Media.
25. Carlin, B.P. and T.A. Louis, *Bayes and empirical Bayes methods for data analysis.* Statistics and Computing, 1997. **7**(2): p. 153-154.
26. Li, S.Z., *Markov random field modeling in image analysis*. 2009: Springer Science & Business Media.
27. Bouman, C. and K. Sauer, *A generalized Gaussian image model for edge-preserving MAP estimation.* IEEE Transactions on Image Processing, 1993. **2**(3): p. 296-310.
28. Herman, G.T., et al., *On the Bayesian approach to image reconstruction.* Information and Control, 1979. **42**(1): p. 60-71.
29. Levitan, E. and G.T. Herman, *A maximum a posteriori probability expectation maximization algorithm for image reconstruction in emission tomography.* IEEE Transactions on Medical Imaging, 1987. **6**(3): p. 185-192.
30. Rosenthal, A., D. Razansky, and V. Ntziachristos, *Fast semi-analytical model-based acoustic inversion for quantitative optoacoustic tomography.* IEEE transactions on medical imaging, 2010. **29**(6): p. 1275-1285.
31. Dean-Ben, X.L., V. Ntziachristos, and D. Razansky, *Acceleration of optoacoustic model-based reconstruction using angular image discretization.* IEEE Transactions on medical imaging, 2012. **31**(5): p. 1154-1162.
32. Dima, A., N.C. Burton, and V. Ntziachristos, *Multispectral optoacoustic tomography at 64, 128, and 256 channels.* Journal of biomedical optics, 2014. **19**(3): p. 036021-036021.
33. Lutzweiler, C. and D. Razansky, *Optoacoustic imaging and tomography: reconstruction approaches and outstanding challenges in image performance and quantification.* Sensors, 2013. **13**(6): p. 7345-7384.
34. Zhang, G., et al., *MAP estimation with structural priors for fluorescence molecular tomography.* Physics in medicine and biology, 2012. **58**(2): p. 351.
35. Luke, G.P., S.Y. Nam, and S.Y. Emelianov, *Optical wavelength selection for improved spectroscopic photoacoustic imaging.* Photoacoustics, 2013. **1**(2): p. 36-42.
36. Kirchner, T., J. Gröhl, and L. Maier-Hein, *Local context encoding enables machine learning-based quantitative photoacoustics.* arXiv preprint arXiv:1706.03595, 2017.
37. Hauptmann, A., et al., *Model based learning for accelerated, limited-view 3D photoacoustic tomography.* arXiv preprint arXiv:1708.09832, 2017.